Journal of Structural Geology 31 (2009) 1525–1539

Contents lists available at ScienceDirect

Journal of Structural Geology

journal homepage: www.elsevier.com/locate/jsg

Interpreting fold and fault geometries from within the lateral to oblique parts of slumps: A case study from the Anglo-Brabant Deformation Belt (Belgium)

Timothy N. Debacker*, Mathijs Dumon, Anouk Matthys

Geology & Pedology, Universiteit Gent, Krijgslaan 281, S8, B-9000 Gent, Belgium

ARTICLE INFO

Article history:
Received 8 April 2009
Received in revised form
1 September 2009
Accepted 4 September 2009
Available online 11 September 2009

Keywords:
Brabant Massif
Cleavage/fold relationships
Fault
Ordovician
Palaeoslope
Slump

ABSTRACT

Using a rigorous comparison of as many slump fold-based and slump-related fault-based methods as possible, also small complex data-sets can be used to deduce a reliable slump transport direction and sense. This is exemplified using late Early Ordovician to Middle Ordovician slump features of the Anglo-Brabant Deformation Belt. The suggested procedure involves (A) an analysis of fold data by means of (1) the mean axis method, (2) the separation arc method, (3) the axial–planar intersection method, (4) the fold hinge azimuth and interlimb angle method, (5) the fold axial surface strike and interlimb angle method and (6) the axial surface dip and dip direction method, (B) an analysis of slump-related fault data by means of (1) the mean fault orientation method, (2) the fault separation method, (3) the fault intersection method and (4) the best-fit girdle to fault poles method, and finally (C) a rigorous comparison of the results of the different methods.

Several possible diagnostic criteria are put forward for distinguishing slump deformation features trending at low angles to transport direction (oblique to lateral parts of slump sheets or internal lobes or tongues) and slump deformation features trending at high angles to transport direction (frontal to central parts of slump sheets). These criteria include the relationship between fold interlimb angle and axial surface dip, the plunge of the fanning axis of the reverse slump-related faults and the plunge of the intersection of the reverse and normal slump-related faults. Such criteria greatly facilitate the interpretation of the often confusing results of many classical methods. Moreover, the plunge azimuth of the intersection of the normal and reverse slump-related faults and the mismatch between slump transport direction inferred from fold-based and fault-based methods, may both be diagnostic for dextrally deformed or sinistrally deformed slump sheet parts.

1. Introduction

Since Jones' (1939) suggestion that an intimate relationship exists between palaeoslope dip direction and slump fold orientation, many studies have used slump folds for determining palaeoslope orientation. This, however, is not an easy task. The complexity of deducing slump transport direction and palaeoslope orientation from slump fold geometries can be attributed to several factors. Firstly, slump folds will not always be oriented subperpendicular to the slump transport direction (e.g. Hansen, 1965; Lajoie, 1972). This is the case, in particular, within the poorly documented lateral parts of slump sheets or internal tongues or lobes (e.g. Woodcock, 1979) (Fig. 1). Secondly, often slump folds occur with an asymmetry opposite to that of the slump sheet movement sense (e.g. Woodcock, 1976a; Strachan and Alsop, 2006). Such folds can be difficult to distinguish from folds with a synthetic asymmetry with respect to slump sense. Thirdly, when deducing slump transport from slump features, one is often hindered by the scale of observation relative to the size of the slump sheet. In an attempt to overcome these problems, many different methods have been developed (see Woodcock, 1979; Bradley and Hanson, 1998; Strachan and Alsop, 2006). All these methods essentially involve a statistical analysis of a very large number of slump fold data.

Unfortunately, in the field geologists are usually confronted with a small and sometimes quite complex data-set of slump-related deformation features. The reason for this usually lies in the combination of a poor degree of exposure and an overprinting by later, hard-rock tectonic deformation. This holds true, in particular, within Palaeozoic and older deformation belts. In such regions, often slump folds are difficult to distinguish from later, hard-rock tectonic folds, and even when they are successfully distinguished,

* Corresponding author. Tel.: +32 9 264 46 09.
E-mail address: timothy.debacker@ugent.be (T.N. Debacker).

0191-8141/$ – see front matter © 2009 Elsevier Ltd. All rights reserved.
doi:10.1016/j.jsg.2009.09.002

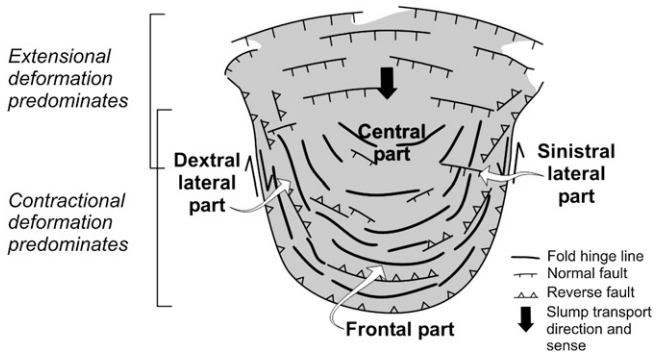

Fig. 1. Cartoon sketch of a slump sheet (grey), showing internal extensional and compressional deformation features and the position of the central, lateral and frontal parts (after Farrell, 1984; Farrell and Eaton, 1987; Bradley and Hanson, 1998).

the data-set may seem too small or too complex for deducing slump transport. However, also these data – however small and fragmented they are – should be taken into account in regional or palaeobasin analytical studies. This particularly concerns data-sets of slump deformation features associated with the lateral parts of slump sheets or lobes (Fig. 1). Although the large-scale, three-dimensional geometry of recent slump sheets has been documented repeatedly in offshore studies, detailed outcrop observations from the lateral parts of ancient (onshore) slump sheets or internal tongues or lobes are virtually non-existent.

In this paper we analyse a small, complex data-set of slump-related deformation features from the upper Lower to Middle Ordovician of the Belgian part of the Anglo-Brabant Deformation Belt. The data-set is analysed using a combination of existing and new fold-based and fault-based methods, and several possible diagnostic criteria for lateral to oblique parts of slump sheets or internal tongues are put forward.

2. Geological setting

The outcrop section occurs in an E–W-trending sunken path at Thy, situated within the Dyle outcrop area of the low-grade, Lower Palaeozoic Brabant Massif (Belgium) (Fig. 2). The Brabant Massif represents the southeastern extension of the Anglo-Brabant Deformation Belt, one of the deformation belts of the Avalon Terrane Assemblage (Verniers et al., 2002). At present, there is only evidence for a single-phase progressive deformation, which took place between the Llandovery and the Givetian (Debacker et al., 2005a; cf. Carney et al., 2008).

The outcrop section mainly consists of deposits of the upper Lower to Middle Ordovician Abbaye-de-Villers Formation (upper Floian to lower Darriwilian; Verniers et al., 2001; Vanmeirhaeghe, 2006). The upper Lower to Middle Ordovician of the Brabant Massif hosts a large number of slump features, formed by slumping along a S-dipping palaeoslope of regional extent (Debacker and De Meester, 2009; see also Debacker, 2001; Beckers, 2003, 2004; Beckers and Debacker, 2006) (Fig. 2). This abundance of slump features may be due to seismic activity related to normal faulting accompanying the separation of the Avalon Terrane Assemblage from Gondwana (Debacker and De Meester, 2009), which commenced during the middle or late Early Ordovician (Verniers et al., 2002). As an alternative cause for slumping, also a Middle Ordovician (early Darriwilian) high meteorite influx is possible (cf. Parnell, 2009).

3. Lithology and overall geometry

The outcrop section is situated between 35 m and 95 m to the west of the junction of the sunken path with the Chemin de Thy, at the NW-corner of Thy castle. All distances are measured starting from this junction (Fig. 3).

In the westernmost part of the section, between 35 and 39.5 m, the lower Tremadocian Chevlipont Formation occurs (cf. Herbosch and Vanguestaine, 1994). These deposits, interpreted as low-density turbidite deposits (Herbosch et al., 1991; Verniers et al., 2001), are separated from the Abbaye-de-Villers Formation by a N–S-trending, oblique normal fault with a dextral component.

The deposits of the Abbaye-de-Villers Formation, constituting the main part of the outcrop section, consist of an alternation of fine sandstone and silty mudstone (Fig. 4A, B). The sandstone, occurring in beds a few millimetres to a few decimetres thick, is rich in

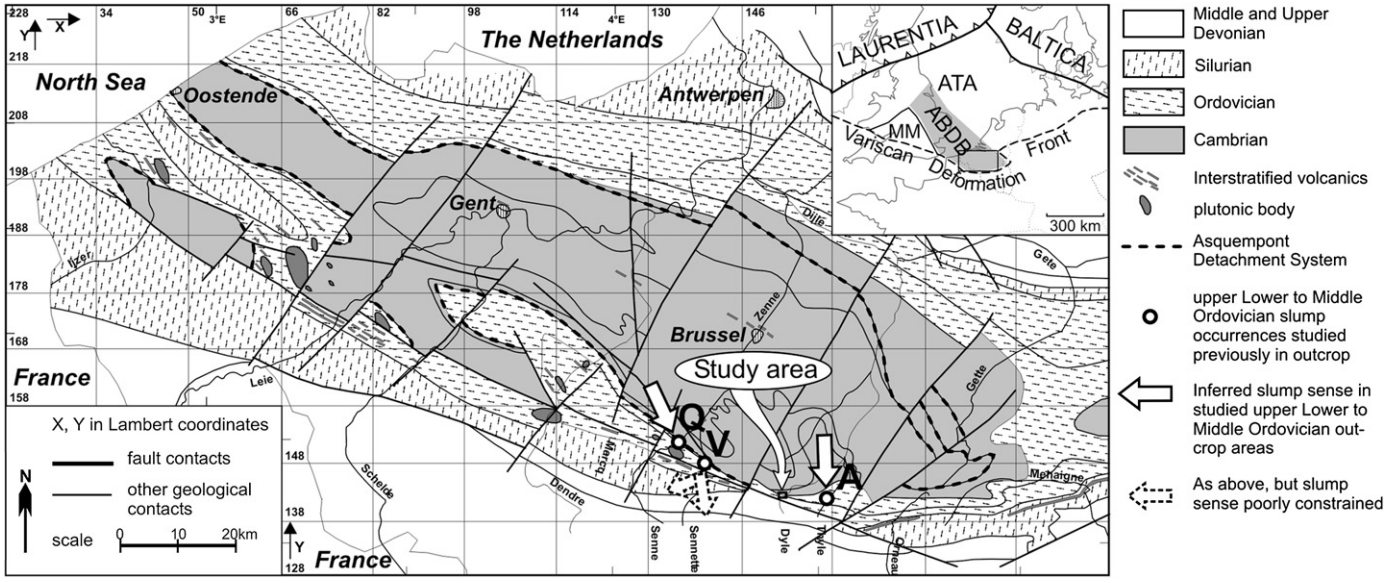

Fig. 2. Geological subcrop map of the Brabant Massif, with position of the study area (after De Vos et al., 1993; Van Grootel et al., 1997). The upper right inset shows the Brabant Massif within Avalonia (ATA), as the southeastern part of the Anglo-Brabant Deformation Belt (ABDB), flanking the Midlands Microcraton (MM). Also shown is the position of three other upper Lower to Middle Ordovician slump occurrences, with inferred slump direction and sense: A: Abbey of Villers-la-Ville (Beckers, 2003, 2004; Beckers and Debacker, 2006), V: Virginal (Debacker, 2001; Debacker et al., 2003), Q: Quenast (Debacker and De Meester, 2009).

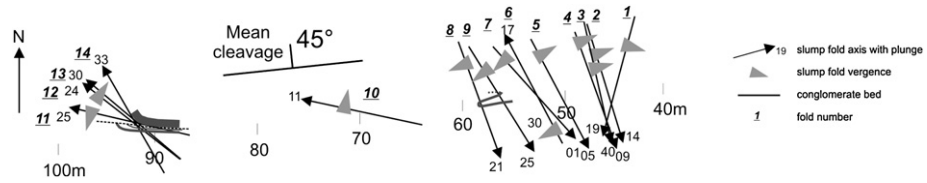

Fig. 3. Spatial occurrence, orientation and asymmetry of the small pre-cleavage folds along the outcrop section. Also mean cleavage orientation and the occurrence of the four conglomerate beds have been added.

bedding-parallel mica. Characteristically, the contacts between sandstone and mudstone are vague and often quite irregular. Moreover, the thin sandstone beds very often have a lenticular nature and the deposits are bioturbated. This formation is thought to have been deposited in a rather shallow environment ranging from the mid to inner shelf (Herbosch, pers. comm.; Vanmeirhaeghe, 2006).

In the outcrop part occupied by the Abbaye-de-Villers Formation many folds and faults occur. Despite this abundance of deformation features, the overall bedding, referred to below as mean regular bedding, dips gently to moderately south between 35 and 75 m. In the rock face in the western part of the section, between 80 and 90 m, bedding dips steeply south. Directly northwest of this, in the path floor between 90 and 95 m, bedding changes from steeply S-dipping, over moderately SW-dipping to moderately to gently W-dipping, thus reflecting an antiformal fold closure (Fig. 3; fold S1).

Within the Abbaye-de-Villers Formation at least four conglomerate levels occur (Figs. 3 and 4C–E). Three of these occur in the western part of the section between 80 and 95 m, where they follow the overall bedding disposition (fold S1). Judging from the position, this three conglomerates sequence (A–C; Figs. 5F,G) actually corresponds to the supposedly ~2 m thick, so-called "Thy conglomerate" of De Magnée and Lambeau (1965). The fourth conglomerate bed (D) occurs in the eastern part of the section, between 54 and 57 m. This conglomerate bed is deformed into a strongly asymmetric fold pair (folds 8 and 9; Fig. 5D). All four conglomerates are fine-grained (clasts always less than 2 cm) and range from clast-supported to matrix-supported (Fig. 4C–E). No grading is observed and the silty matrix is similar to that of the surrounding beds. Three main clast types occur, all of which are usually subparallel to bedding. These are, in decreasing order of abundance 1) black, rounded to subangular, ellipsoidal phosphate nodules, 2) angular, elongate clasts of siltstone to sandstone, with the same mineralogical composition as that of the surrounding beds, and 3) subangular monocrystalline quartz fragments, never exceeding three millimetres in diameter (De Magnée and Lambeau, 1965). Although clearly of intraformational origin (De Magnée and Lambeau, 1965; cf. Herbosch and Vanguestaine, 1994), the geological significance of these conglomerates is still unknown.

4. Structural field observations

4.1. Folds and cleavage/fold relationships

Many small-scale folds occur (half wavelengths <3 m). The vast majority of these are characterised by a pronounced fold asymmetry, which may vary between neighbouring, similar-sized folds (Figs. 3 and 5; Table 1).

Throughout the section, cleavage has an E–W-trend and dips moderately to gently north, similar to cleavage orientation in other parts of the Dyle outcrop area (Fig. 6; Herbosch and Lemonne, 2000; Debacker et al., 2005b; Beckers and Debacker, 2006). Most small-scale folds, however, have a completely different orientation, trending NW–SE (folds 1–14; Figs. 3 and 6). Cleavage is oblique to these fold axial surfaces, and shows the same refraction sense on opposite fold limbs, indicating folding prior to cleavage development. A further characteristic of these pre-cleavage small-scale folds is the fact that they are often separated from relatively undeformed overlying beds by faults, usually of a welded nature (Fig. 5).

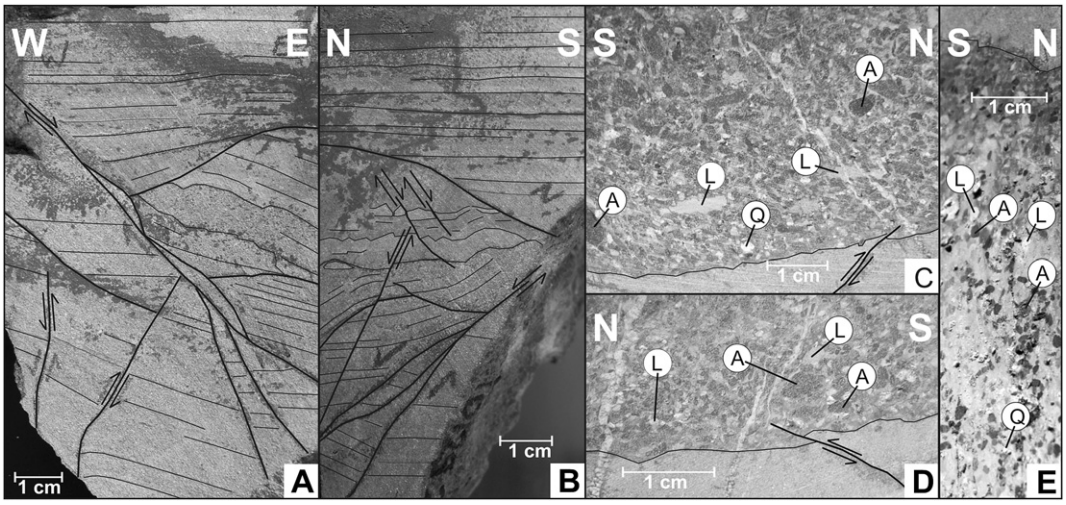

Fig. 4. Photographs of selected lithologies and small-scale soft-sediment deformation features within the Abbaye-de-Villers Formation. A and B) Laminated siltstone to fine-grained sandstone, affected by pre-cleavage normal faults and truncation surfaces. Note changes in bedding thickness and presence of disrupted sediments, indicating faulting prior to lithification (sample TD1292; at 41 m). C and D) Conglomerate bed B, with underlying sandstone bed. L: lithic fragment, A: apatite nodule, Q: quartz. Note quartz veins oriented at high angles to bedding, affected by cleavage and compaction fabric. Also note pre-cleavage reverse fault (sample TD1282; at 93 m). E) Overturned conglomerate bed D, with underlying sandstone bed (top of photo). A, Q and L as in C and D (sample TD1296; at 55 m).

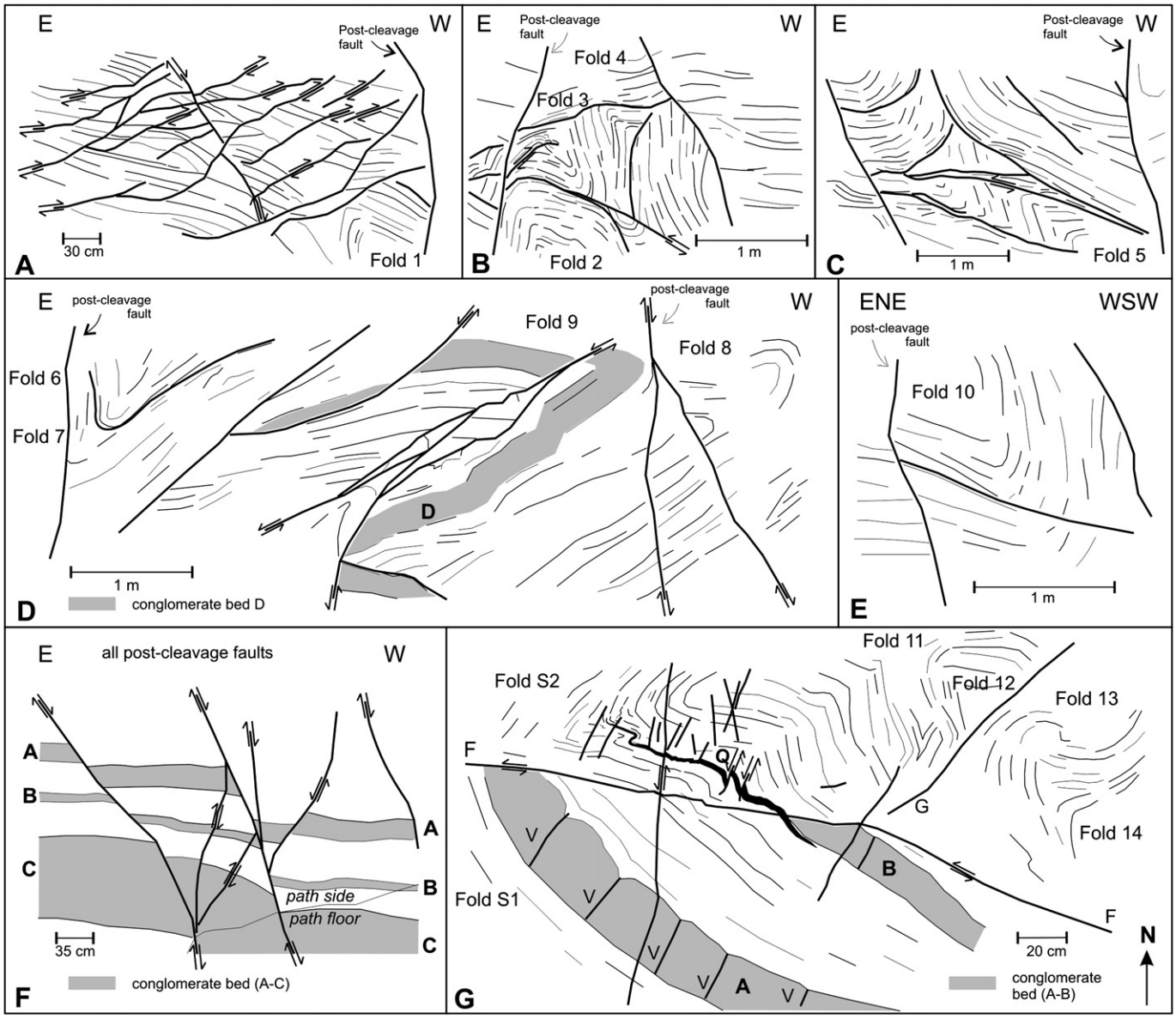

Fig. 5. Line drawings of deformation geometries observed in outcrop. All faults, detachments and truncation surfaces (thick lines) have a pre-cleavage origin, unless stated otherwise. A) Small-scale pre-cleavage faults and pre-cleavage fold 1 (43–45 m). B) Pre-cleavage folds 2–4 (45–48 m). C) Pre-cleavage fold 5 and related deformation (49–52.5 m). D) Pre-cleavage folds 6–9, with folded conglomerate bed D (52.5–58.5 m). E) Pre-cleavage fold 10 (70–72 m). F) Steeply to moderately S-dipping conglomerate beds A–C, affected by steep, post-cleavage normal faults (90–92 m). G) Conglomerate beds A and B, pre-cleavage faults F and G, quartz vein Q, syn-cleavage folds S1 and S2 and pre-cleavage folds 11–14 in the path floor outcrop (92.5–95 m). V: veins formed at high angles to bedding, prior to cleavage (see Fig. 4C and D), but sometimes re-used by later post-cleavage faults. Except for faults F, G and the veins, all faults and fractures have a post-cleavage origin.

In the western part of the section, fold S1 represents a larger-scale, moderately W-plunging, moderately inclined, asymmetric, south-verging antiform (Figs. 3 and 5G). As cleavage dip is close to the inferred dip of the axial surface, and the cleavage poles plot on the best-fit girdle to the bedding poles, this fold may have formed during cleavage development. To the north of fault F, which truncates conglomerate beds A and B, a finely laminated, strongly folded sequence occurs (Fig. 5G). The upper, stratigraphically youngest part of this sequence contains a gently W-plunging, steeply inclined, asymmetric, south-verging antiform (fold S2; Fig. 5G). Cleavage is subparallel to the fold axial surface and shows opposite refraction senses on opposite limbs, suggesting a syn-cleavage fold origin. Below this fold, several more small-scale asymmetric folds occur (folds 11–14), of which the hinge lines plunge gently to moderately to the NW, oblique to regional strike, to cleavage and to folds S1 and S2 (Fig. 6). The axial surfaces of these folds are curved, they are cross-cut by cleavage and at least one of these folds is refolded by a small, parasitic fold of fold S2 (Fig. 5G). This implies development of these folds prior to cleavage and to fold S2.

4.2. Faults

A first group of faults, with a post-cleavage origin, consists of moderately to steeply dipping, NW–SE to NNE–SSW-trending faults, oriented at high angles to regional strike and to mean regular bedding (Fig. 5F, G). As the hanging wall and footwall are not welded together and fault traces are relatively straight, regardless of surrounding bedding orientation, these faults are readily apparent in outcrop. Occasionally, a quartz infill occurs and

Table 1
Bedding and fold data of 14 pre-cleavage folds. Mean regular bedding is the relatively undeformed, more or less uniformly dipping bedding surrounding these pre-cleavage folds.

Fold	Mean regular bedding	Fold β-axis	Fold axial surface	Interlimb angle	Fold asymmetry (− clockwise looking down-plunge)	Fold asymmetry
1	073/28S	19/195; $n=5$	184/62W	57°	+	Top-to-southeast
2	092/17S	14/163; $n=4$	146/41SW	59°	+	Top-to-east
3	092/17S	40/167; $n=5$	127/53S	39°	+	Top-to-east
4	092/17S	09/160; $n=5$	148/38SW	73°	+	Top-to-east
5	138/27SW	05/152; $n=7$	147/45SW	34°	+	Top-to-northeast
6	314/16NE	17/332; $n=5$	327/75NE	43°	+	Top-to-southwest
7	314/16NE	01/138; $n=5$	/	66°	−	Top-to-southwest
8	134/21SW	21/160; $n=6$	012/53E	92°	−	Top-to-west
9	134/21SW	25/148; $n=5$	044/26SE	50°	−	Top-to-southwest
10	086/50S	11/282; $n=15$	104/80S	63°	−	Top-to-north
11	128/59SW	25/283; $n=6$	196/25 W	26°	+	Top-to-south
12	128/59SW	24/308; $n=6$	157/30SW	123°	−	Top-to-northeast
13	128/59SW	30/310; $n=4$	307/85NE	117°	No asymmetry	No asymmetry
14	128/59SW	33/330; $n=7$	150/90SW	89°	No asymmetry	No asymmetry

sometimes slickenlines can be observed, reflecting an oblique normal movement with a dextral component. The fault separating the Chevlipont Formation and the Abbaye-de-Villers Formation belongs to this first group of faults, as well as the faults displacing conglomerate beds A–C in the western part of the outcrop (Fig. 5F).

The second group of faults, observed both in outcrop and in hand samples, occurs at variable angles to bedding. Some of these are oriented at low angles to bedding and are referred to as detachments. Most trend at high angles to regional strike, similar to those of the first group. A very characteristic feature is the fact that the rock often remains cohesive across the faults ("welded" faults), making these faults difficult to distinguish (e.g. Fig. 4A, B). Often, especially in the case of the detachments, fault traces are curved. In such cases, fault curvature reflects the curvature of the folded, overlying beds, thus suggesting a relationship between the faults and the small-scale pre-cleavage folds (Fig. 5B–D). None of these faults has associated veins. In addition, these faults are cross-cut by cleavage. Moreover, they are often flanked by disrupted sediments, indicating formation prior to lithification (e.g. Fig. 4A, B). Because of the absence of slickenlines, the scarcity of marker horizons and the complex deformation style, direction, sense and amount of displacement are often difficult to estimate. Nevertheless, in terms of relative displacement, both reverse and normal faults can be recognised. Cross-cutting relationships between normal and reverse faults were not observed. In many cases, the amount of displacement along individual faults appears to be minor (mm- to cm-scale; e.g. Fig. 5A). In the case of fault F, however, observed in the path floor in the western extremity of the outcrop, a much larger displacement took place (at least 1.5 m; Fig. 5G). This fault is cross-cut by a bedding-parallel quartz vein (Q) that is folded by syn-cleavage fold S2, thus confirming the pre-cleavage origin of fault F.

5. Interpretation of structural field observations

5.1. Relative chronology and overall structure

Two folding events occurred. A first event, which took place prior to cleavage development, resulted in predominantly NW–SE-trending folds (folds 1–14). As these folds not only deform pre-cleavage detachments, but are also truncated by these detachments and other pre-cleavage faults (faults of the second group), the pre-cleavage folds and faults (both normal and reverse) are considered to have formed cogenetically (see Fig. 5). This was followed by the local development of bedding-perpendicular quartz veins, which were later deformed by bedding-normal compaction (e.g. Figs. 4C, D and 5G). The second folding event, initially leading to the local development of bedding-parallel quartz veins (e.g. vein Q, Fig. 5G), resulted in E–W-trending, south-verging, syn-cleavage buckle folds (folds S1 and S2). The last features to have formed are steep oblique normal faults, referred to above as faults of the first group.

The outcrop section is oriented at low angles to the hinge of a decametre-scale or larger, ~E–W-trending, south-verging, syn-cleavage fold with a stepfold geometry. The conglomerates between 90 and 95 m are situated within the antiformal closure (fold S1). In the rock face between 65 and 90 m, the steeply S-dipping southern limb is exposed. The eastern section part corresponds to a gently S-dipping limb, close to the fold hinge zone.

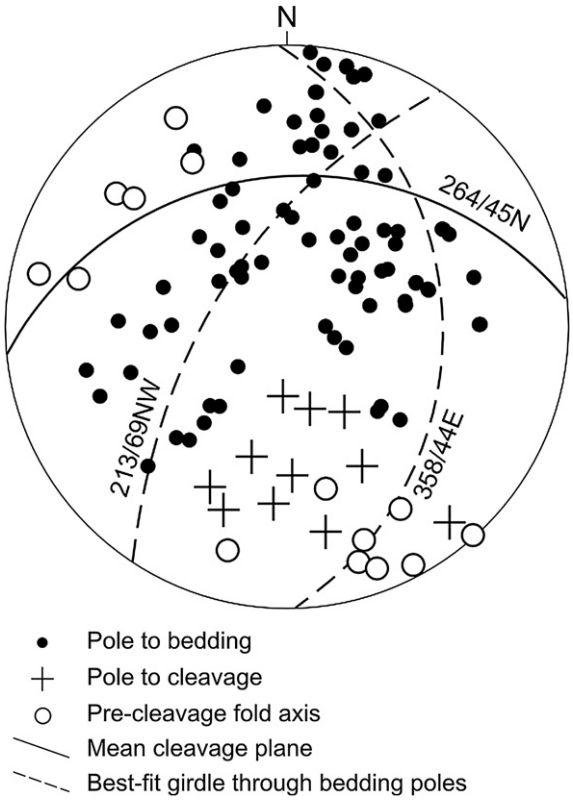

Fig. 6. Lower-hemisphere equal-area projection of poles to regional bedding with two (!) best-fit girdles, poles to cleavage, mean cleavage plane (264/45N), and pre-cleavage fold axes. The fact that two girdles to bedding poles are shown is because of the non-cylindrical nature of the overall syn-cleavage fold: syn-cleavage fold hinge line of 21/123 in E-part of section (girdle: 213/69NW) and 46/268 in W-part (girdle: 358/44E).

Table 2
Restoration of pre-cleavage fold axes and axial surfaces to their initial orientation prior to syn-cleavage folding. Values used for untilting: +21° rotation around 00/213 for folds 1–10 and −46° around 00/178 for folds 11–14. For unfolding, an axis of 00/123 is used for folds 1–10 and 00/268 for folds 11–14. Unfolding angles are controlled by local mean regular bedding (MRB). Rotation convention: (+) is anticlockwise (clockwise) viewed own-plunge. Fold asymmetry: (−) is clockwise looking down-plunge.

Fold	Untilted MRB	Untilted β-axis	Untilted axial surface	Unfolding	Unfolded β-axis	Unfolded axial surface	Asymmetry
1	119/18S	11/190	187/81W	−18° ar. 00/123	06/010	191/74W	−
2	162/19W	02/342	163/52SW	−15° ar. 00/123	11/341	173/41W	−
3	162/19W	24/159	142/57SW	−15° ar. 00/123	15/163	147/43SW	+
4	162/19W	08/340	166/50W	−15° ar. 00/123	17/337	177/40W	−
5	167/38W	13/333	162/56SW	−22° ar. 00/123	23/327	176/41W	−
6	255/24N	35/337	320/68NE	17° ar. 00/123	24/345	323/52NE	+
7	255/24N	19/319	/	17° ar. 00/123	14/324	/	+
8	172/32W	04/157	002/34E	−22° ar. 00/123	08/336	343/49E	+
9	172/32W	06/146	079/07S	−22° ar. 00/123	03/327	319/18NE	+
10	105/40S	30/279	109/74S	−39° ar. 00/123	10/266	100/37S	−
11	089/41S	20/102	339/23NE	41° ar. 00/268	06/111	296/52NE	−
12	089/41S	13/125	029/20SE	41° ar. 00/268	12/305	299/34NE	−
13	089/41S	07/124	121/67SW	41° ar. 00/268	17/301	145/37SW	?
14	089/41S	05/316	141/51SW	41° ar. 00/268	33/305	184/39W	?

As shown in Fig. 6, this fold is non-cylindrical, and has a pronounced periclinal nature. To the west, the antiformal closure plunges moderately towards 268°, whereas to the east, bedding orientation suggests an antiform with a gentle plunge towards 123°.

5.2. Origin of the pre-cleavage folds and related features

The pre-cleavage folds (folds 1–14) and pre-cleavage faults either formed during an older, thus far unknown, pre-cleavage tectonic deformation phase, or are a result of slumping (cf. Debacker et al., 2001). In the study area, as well as in the other parts of the Brabant Massif, there is no evidence for more than one tectonic deformation phase (e.g. Sintubin, 1997, 1999; Debacker, 2001; Verniers et al., 2002; Debacker et al., 2001, 2005a, 2006, and references therein). By contrast, the pre-cleavage folds do have characteristics commonly attributed to slump folds. These are the isolated, intraformational position between non-folded beds (e.g. Fig. 5C), the truncation of folds by overlying, younger beds (e.g. Fig. 5A, E and G), the dispersed orientation of the fold axes (Fig. 6), the often irregular fold shape (e.g. Fig. 5G), the association with other soft-sediment deformation features such as welded faults and disrupted sediments (e.g. Fig. 5B–D), and the absence of fold-related veins or cleavage (cf. Jones, 1939; Kuenen, 1949; Helwig, 1970; Corbett, 1973; Woodcock, 1976a; Rupke, 1976; Elliott and Williams, 1988). Moreover, also in other outcrop areas of the Brabant Massif, upper Lower to Middle Ordovician slump deformation features frequently occur (e.g. Legrand, 1968; Michot, 1977; Debacker, 2001; Debacker et al., 2003; Beckers, 2003, 2004; Beckers and Debacker, 2006). For these reasons, the pre-cleavage folds and pre-cleavage faults are interpreted as slump-related deformation features. In this respect, the conglomerate levels may well correspond to debris flow deposits formed during earlier stages of progressive slope failure.

6. Inferring slump direction and sense

Many methods exist for deducing slump transport direction and sense on the basis of slump fold data, all of which have their specific advantages and draw-backs (Woodcock, 1979; Strachan and Alsop, 2006). Especially for small data-sets, as in this case, as many methods as possible should be used. Here we employ six slump fold-based methods, being 1) the mean axis method, 2) the separation arc method, 3) the axial surface intersection method, 4) the fold hinge azimuth and interlimb angle method, 5) the axial surface strike and interlimb angle method and 6) the axial surface dip and dip direction method. Methods 1–4 have been used previously (e.g. Woodcock, 1979; Strachan and Alsop, 2006, and references therein). Method 5 is based on method 4 (Strachan and Alsop, 2006), but uses axial surface strike instead. As far as the authors are aware of, method 6 has not been applied previously. In addition, we also propose several methods based on slump-related faults.

In all cases, slump data (fold axes, axial surfaces, faults…) have to be restored to their probable orientation prior to tectonic, cleavage-related folding. In order to do so, two consecutive rotations are performed. In the first rotation, referred to as untilting, the plunge of the regional, syn-cleavage fold axis is removed. In the second rotation, referred to as unfolding, the limbs (i.e. mean regular bedding) of the untilted syn-cleavage fold are unfolded (i.e. restored to horizontal) around the untilted, regional, syn-cleavage fold axis (Table 2). A complexity arises when the regional, syn-cleavage fold is not cylindrical. In such cases, the use of a (virtual) mean fold axis should be avoided as this may result in an incorrect final orientation. A better approach is to split up the outcrops or observation points into two or more groups of which the regular bedding points to a local, syn-cleavage fold with a higher degree of cylindricity. For each of these groups a different value for untilting and unfolding is used, depending on the local syn-cleavage fold axis. In this study, the main, eastern part of the outcrop is characterised by a gently SE-plunging fold axis (21/123), whereas the western part of the outcrop is characterised by a moderately W-plunging fold axis (46/268) (see Fig. 6). Even with this correction, during restoration an error cannot be avoided. As the mean regular bedding and the local syn-cleavage fold axis have been double-checked, as the syn-cleavage fold is not steeply plunging and as all slump features analysed are situated close to the hinge zone of the syn-cleavage fold, this error is estimated at less than 10°.

6.1. Methods based on slump fold data

6.1.1. Mean axis method

The (along-slope) mean axis method, proposed by Jones (1939; cf. Hahn, 1913), is based on the idea that slump fold axes statistically are parallel to the strike of the palaeoslope and perpendicular to the slump direction. Slump sense is inferred from regional constraints (e.g. Jones, 1939) or from fold vergence (e.g. Crimes, 1970; Woodcock, 1976b).

For our data, a mean slump fold axis with azimuth of 324° ± 026° is obtained (Fig. 7A). In the along-slope mean axis method this would suggest slumping along a direction of 054°–234° (±026°). However, two uncertainties exist. Firstly, opposite asymmetries are observed for folds with similar fold axis orientations (Tables 1 and 2 and Fig. 7B). This may be due to the presence

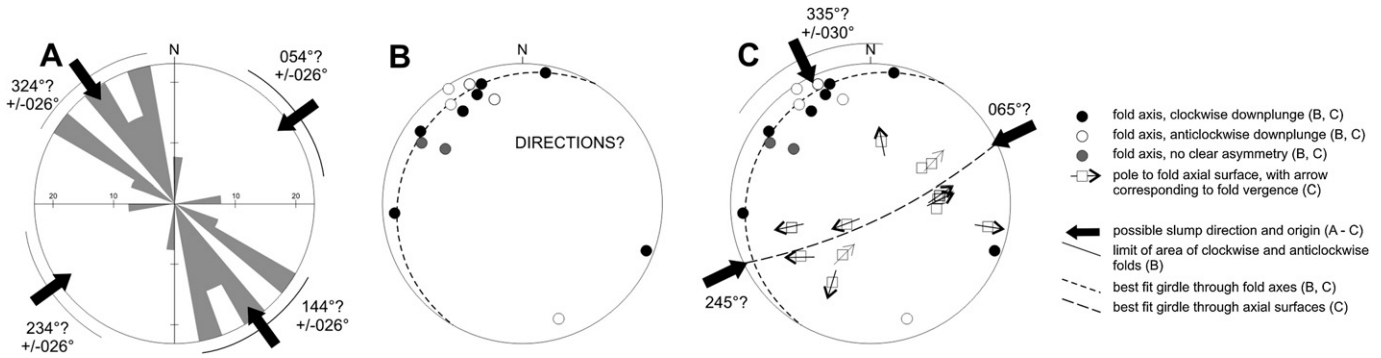

Fig. 7. A) Mean axis method: rose plot of slump fold axes with four possible solutions, depending on whether down-slope or along-slope average axes are observed. B) Separation arc method: lower-hemisphere equal-area projection of slump fold axes, with sense of fold asymmetry indicated. C) Axial–planar intersection method: lower-hemisphere equal-area projection of slump fold axial surfaces, with fold asymmetry indicated. For clarity, also slump fold axes are added. Also shown are three possible slump senses, two assuming axial surface fanning parallel to palaeoslope trend and one assuming a fanning axis at low angles to slump transport direction. See text.

of a) minor parasitic folds on the short, inverted limbs of larger folds or b) folds with an upslope vergence, formed by back-thrusting or back-folding (Woodcock, 1976a; Blay et al., 1977; Strachan and Alsop, 2006). As the former (a) was taken into account during fieldwork, and the vast majority of the folds analysed have similar sizes, disturbing effects of parasitic folds are unlikely. The latter (b) is more problematic. As the number of folds with a top-to-the-NE asymmetry is comparable to the number of folds with a top-to-the-SW asymmetry, slump sense cannot be concluded. Secondly, as pointed out by Woodcock (1979), the mean axis will not always parallel the palaeoslope trend and distributions with down-slope average axes do exist. Especially within the lateral parts of a slump sheet or tongue, the mean axis may be closer to the palaeoslope dip direction than to the palaeoslope strike (Woodcock, 1979; cf. Lajoie, 1972). In this case, slumping could also be along a direction 144°–324° (±026°), again with an unknown sense.

For our data it is difficult to tell whether the mean axis has an along-slope or a down-slope orientation and therefore at least four different slump senses are possible (Fig. 7A).

6.1.2. Separation arc method

The separation arc method, initially proposed by Hansen (1965, 1967, 1971), is based on the observation that, during down-slope translation, folds tend to rotate towards the slump transport direction, away from the palaeoslope strike (cf. Lajoie, 1972). This results in folds with opposite asymmetry, ideally symmetrical about the slump transport direction. The method consists of outlining fields with similar down-plunge fold asymmetry on an equal-area projection, and constructing the bisector of a "separation arc" or "separation angle" (i.e. a segment of the best-fit girdle to the fold axes; Hansen, 1965; Wheeler, 1975) between fields with opposite down-plunge fold asymmetry.

As shown in Fig. 7B, there virtually is full overlap between fields of clockwise and anticlockwise folds. This might partly be due to back-folding (Woodcock, 1976a; Blay et al., 1977; Strachan and Alsop, 2006), but as the number of folds with a top-to-the-NE asymmetry is comparable to the number of folds with a top-to-the-SW asymmetry, it cannot be ascertained which folds are synthetic and which folds are antithetic with respect to slump sense. As recommended by Woodcock (1979), in such cases this method should not be used.

The best-fit girdle to the slump fold axes, which is subparallel to the mean axial surface (199/16NW) and should be at low angles to the slump sheet or shear plane (e.g. Woodcock, 1979), dips gently to the NW (214/14NW). Such imbrication would seem compatible with slump transport from N, NW or W towards S, SE or E (e.g. Bradley and Hanson, 1998; Smith, 2000). However, despite the latter deduction, the direction remains completely unknown. Hence, for our data-set, the separation arc method cannot be used.

6.1.3. Axial–planar intersection method

As pointed out by Woodcock (1979; cf. 1976a,b), slump fold axial surfaces form a maximum dispersed about the mean slump fold axis, and the mean axial surface is usually imbricated with respect to the slump sheet, dipping in the opposite direction to the palaeoslope. Despite these early observations, the axial–planar intersection method was first used for mid-crustal shear zones (Alsop and Holdsworth, 2002), and was only recently applied to slump folds (Strachan and Alsop, 2006). The method relies on the fact that layer-parallel shear should result in a fanning of the axial surfaces about the strike of the palaeoslope, whereas layer-normal shear should result in a fanning about the palaeoslope dip direction (Strachan and Alsop, 2006; Alsop and Holdsworth, 2007). The former is expected at the frontal parts of a slump sheet, whereas the latter is expected to dominate within the oblique to lateral parts of slump sheets or internal tongues or lobes (cf. Alsop and Holdsworth, 2007).

For our data, the axial surfaces show a rough fanning about 10/335, suggestive of slumping along a direction 065°–245° in the case of layer-parallel shear or along a direction 155°–335° in the case of layer-normal shear (Fig. 7C). The fact that the number of folds with a clockwise asymmetry (7) compares to the number of folds with and anticlockwise asymmetry (5) seems more compatible with layer-normal shear than it does with layer-parallel shear (cf. Strachan and Alsop, 2006) and hence suggests a position with the lateral parts of a slump sheet or internal lobe. Moreover, the mean axial surface dips gently northwest (199/16NW). Combined, this suggests a SE-ward slump transport. Arbitrarily, we suggest slump direction to be situated within an area of 30° on each side of the axial–planar intersection. This would imply slumping from ~335° ± 030° (305°–005°).

6.1.4. Fold hinge azimuth and interlimb angle method

This method, first applied by Strachan and Alsop (2006), relies on the idea that, with applied shear stress, folds tighten as they rotate from an original palaeoslope strike-parallel orientation to a transport-parallel orientation. On a graph of interlimb angle versus hinge line azimuth a slump mass that has undergone no fold axis rotation will plot as two separate fields approximating the palaeoslope trend. By contrast, in case of significant fold axis rotation a V-shaped pattern will emerge with the apex approximating the palaeoslope dip direction (Strachan and Alsop, 2006).

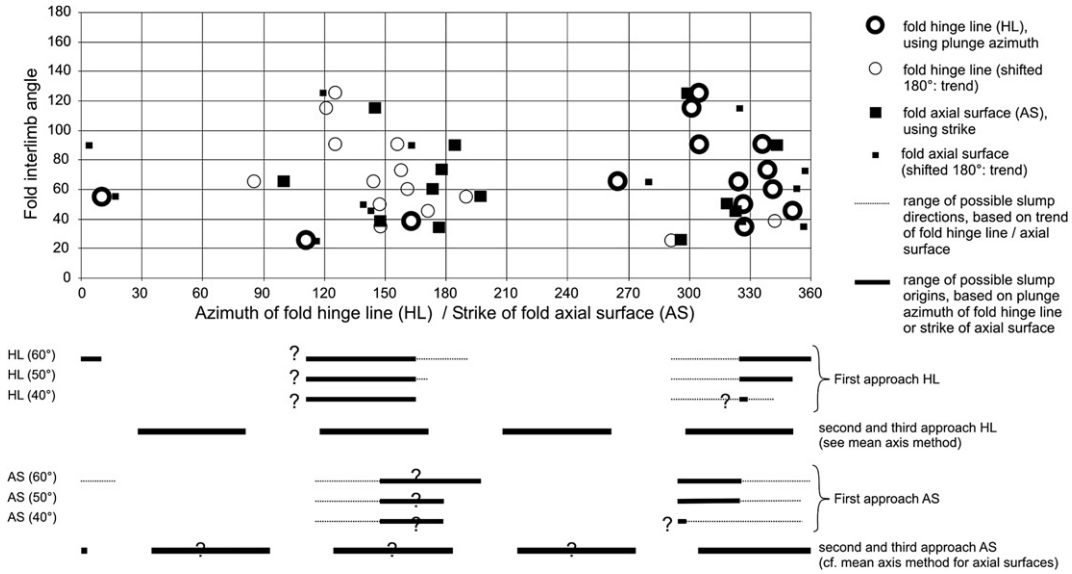

Fig. 8. Graph of fold interlimb angle versus azimuth of fold hinge line plunge and strike of fold axial surface, used in the fold hinge azimuth and interlimb angle method and the fold axial surface strike and interlimb angle method, respectively. Possible slump direction origins are shown below. Note that for each of the two methods, three approaches exist for interpreting the present data-set. See text.

As shown in Fig. 8, there is no clear V-shaped pattern, but neither are there two well-defined clusters (compare with Fig. 10 of Strachan and Alsop, 2006). This can partly be attributed to the small nature of the data-set and to the NW-plunge of the majority of the folds. Because of this, the data can be interpreted in at least three different ways. In a first approach, we assume that the folds with the lowest interlimb angles are indeed closest to transport direction. Seven folds have an interlimb angle equal to or lower than 60°, of which five, with interlimb angles from 60 to 34°, have a plunge azimuth between 320 and 010°, and two, with an interlimb angle of only 26° and 39°, have a plunge azimuth of 111° and 163°. This would suggest slumping along a broad direction of 290°–010° – 110°–190°. If only the five former folds are considered, taking into account the NNW-dip of the best-fit girdle to the slump fold axes (see Fig. 7B and above), the inferred slump sense would be from 320°–010° to 140°–190°. For small data-sets one of the obvious draw-backs concerns pinpointing "small interlimb angles". For this reason, the range of possible slump directions is marked for interlimb angles below 60°, below 50° and below 40°. Such a lowering of the threshold results in smaller possible slump intervals, but at the same time the uncertainty strongly increases (only 3 below 40°). In all cases, a NNW–SSE to NW–SE-directed slump sense is obtained, oriented at low angles to the mean slump fold axis. However, unfortunately, also folds with large interlimb angles plot very close to this interval.

In a second and third approach, the data are interpreted as two separate clusters. The second approach assumes that the clusters approximate the palaeoslope trend (Strachan and Alsop, 2006), whereas the third approach assumes that the clusters approximate the palaeoslope dip direction. The former corresponds to the along-slope mean axis method and the latter to the down-slope mean axis method and hence these two results are the same as those of the mean axis method (see above).

6.1.5. Fold axial surface strike and interlimb angle method

This method is based on that described above, but differs from the latter in the fact that axial surface strike is used instead of fold hinge line azimuth. As we expect that also axial surface strike may change during slumping, hereby becoming closer to slump transport direction (see also axial–planar intersection method), a similar, but non-identical (cf. Smith, 2000), relationship should become apparent as in the case of the fold hinge azimuth and interlimb angle method. In addition, as axial surface strike is linked to axial surface dip direction (strike is 90° anticlockwise of dip direction), it provides extra information about the slump sense.

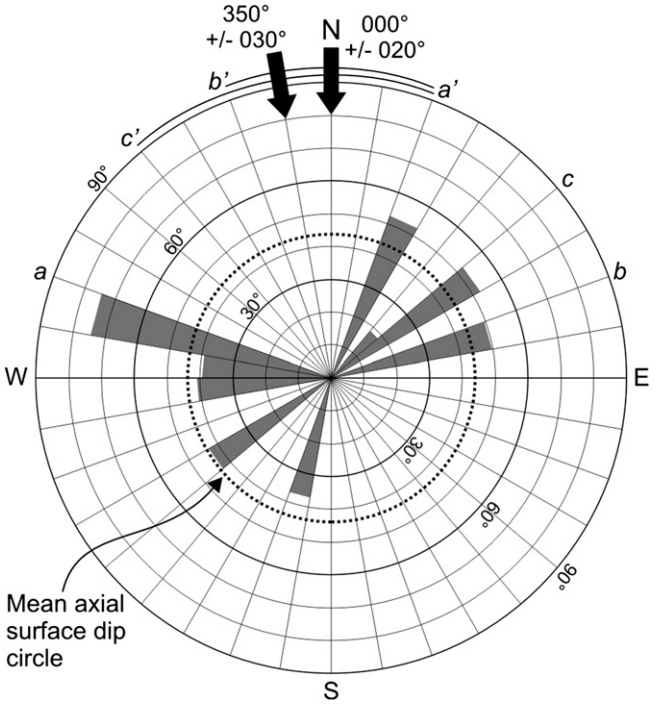

Fig. 9. Rose plot showing axial surface dip direction and axial surface dip, used in the axial surface dip and dip direction method. For clarity, axial surface dip directions used (*a* on the one hand and *b* and *c* on the other hand) and corresponding axial surface trends (*a*′ on the one hand and *b*′ and *c*′ on the other hand) are marked. In each case, not the mean of the dip direction interval but the side of the dip direction interval resulting in the largest possible slump interval is used. As the dip direction intervals of *c* and *b* are close together, and no gently dipping axial surfaces with intermediate dip directions exist, both are marked. However, for final interpretation (see Fig. 10), only those leading to the larger possible slump origin interval are used. Arrows reflect inferred slump sense and origin. See text.

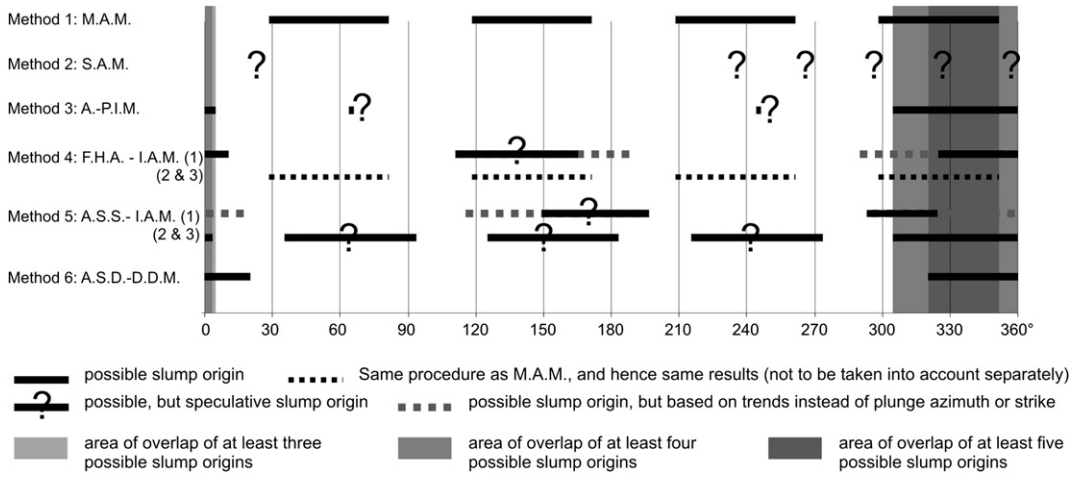

Fig. 10. Summary graph of the six fold-based methods employed, with added areas of overlap for three, four and five possible slump origins. From this graph, we deduce slumping from between 305° and 005° (∼335° ± 030°). M.A.M.: mean axis method; S.A.M.: separation arc method; A.-P.I.M.: axial–planar intersection method; F.H.A.-I.A.M.: fold hinge azimuth and interlimb angle method; A.S.S.-I.A.M.: axial surface strike and interlimb angle method; A.S.D.-D.D.M.: axial surface dip and dip direction method. For methods 4 and 5 numbers 1, 2 and 3 refer to first, second and third approach, respectively. Compare with Figs. 7–9 and see text.

There is no clear V-shaped pattern and neither are the clusters well-defined (Fig. 8). Also here the data can be interpreted in at least three different ways. The first approach assumes that the axial surface trends corresponding to the smallest interlimb angles are closest to slump transport direction. Again, there is an uncertainty on what are "small interlimb angles". For this reason, possible directions are determined for folds with interlimb angles equal to or below 60° ($n = 7$), below 50° ($n = 5$) and below 40° ($n = 3$). This would appear to suggest slumping at low angles to the mean fold axis, along a direction of 295°– 015° – 115°–195°, 295°– 360° – 115°–180° and 295°– 360° – 115°– 180°, respectively. For those folds with an interlimb angle below 60°, three axial surfaces are NE-dipping (strike between 295° and 330°), and four are W-dipping (strike between 145° and 195°). For this reason, slump sense is more likely SSE-ward than NNW-ward, i.e. from 295°–015° to 115°–195° or from 295°–360° to 115°–180° (depending on the threshold used). However, unfortunately, also axial surfaces of folds with large interlimb angles plot in this interval.

In the second approach, in which it is assumed that the clusters approximate the palaeoslope trend (cf. along-slope mean axis method applied to axial surfaces), inferred slump direction would be along 064°–244° (±029°; cf. axial–planar intersection method). In the third approach, in which it is assumed that the clusters are close to palaeoslope dip direction (cf. down-slope mean axis method applied to axial surfaces), inferred slump direction would be along 154°–334° (±029°). As the majority of the axial surfaces are either W-dipping or NE-dipping, the slump sense is more likely SSE-ward, or from 334° ± 029°.

6.1.6. Axial surface dip and dip direction method

Several authors pointed out an analogy between slump and thrust sheets (e.g. Alsop and Holdsworth, 2004, 2007; Maltman, 1994). The lateral parts of thrust sheets usually coincide with lateral ramps or tear faults. At these sites, shear strain caused by thrust movement will result in a steepening of pre-existing axial surfaces and in the formation of folds with axial surfaces steeper than those formed at frontal margins (cf. Coward and Potts, 1983; Coward and Kim, 1981). Also the lateral parts of slump sheets or tongues usually coincide with oblique slip or strike-slip faults (Farrell, 1984; Farrell and Eaton, 1987; Maltman, 1994). Hence, by analogy, due to layer-normal shear within the lateral parts of slumps the axial surfaces trending at low angles to transport direction are expected to be steeper than those trending at higher angles to transport direction (e.g. Alsop and Holdsworth, 2007). If so, within the lateral to oblique parts, slump transport direction should be at low angles to the trend of the steepest axial surfaces.

The method involves plotting dip direction versus dip on a rose plot, arbitrarily using dip direction segments of 010° (Fig. 9). In cases in which steep axial surfaces of slump folds with opposing asymmetries have comparable trends (i.e. strike difference between 90 and 180°), as in this case, slump direction is taken as the bisector of the obtuse angle between the dip directions of the steepest axial surfaces, with slump sense being opposite to the mean dip direction. Also for this method, the results will depend on the threshold used. As a threshold for "steep" axial surfaces, we propose considering all axial surfaces with dips above the mean (here 43°). In case several axial surfaces have roughly the same dip direction (same quadrant on rose plot), we suggest grouping only those having dip directions not coinciding with and/or not being separated by axial surfaces with gentle dips (i.e. less than the mean dip). In order to reduce the risk of errors, for each 010° segment only the extreme dip direction values are taken into account (largest error margins). For our data this suggests slumping from the NNW (350° ± 030°).

6.1.7. Comparing the results of the different fold-based methods

This essential part of the analysis involves graphing the results of the different methods, taking into account the assumptions of each method (Fig. 10). On the basis of overlap of the results of at least three methods, slumping must have taken place from between 305° and 005°, or from 335° ± 030°. Taking into account additional constraints from individual methods, especially those from methods 4, 5 and 6, the probable interval might further be reduced (∼334° ± 029° and ∼335° ± 015°, for overlap of four, respectively five methods).

However, it is important to realise that the final result with the smallest error margin will not necessarily be more trustworthy. Instead, a final solution with larger error margins (several tens of degrees) is more likely to encompass fully the actual slump origin and sense than a final solution with smaller error margins. Because of this, we conclude SSE-ward slumping from 335° ± 030°. An error of ∼30° may seem large, but considering that for these slump folds no additional constraints on strain axes orientation exist, that the data-set is small and complex, that the slump folds have been deformed afterwards, and that slump sheets often have irregular

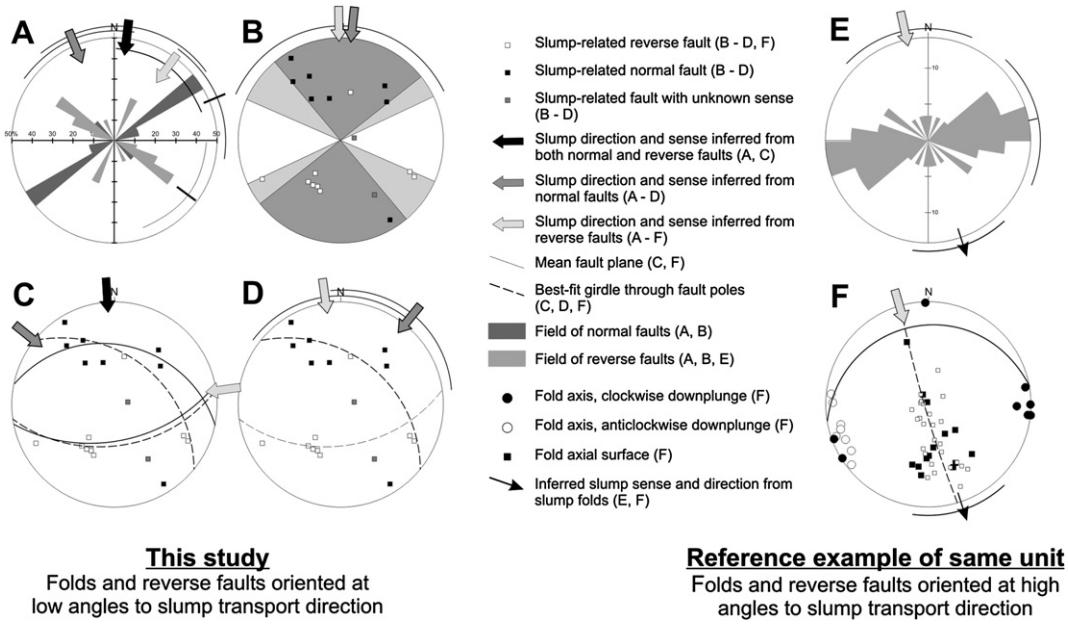

Fig. 11. Four fault-based methods (A–D) applied to the present data-set, with a reference example from the same lithostratigraphic unit from another outcrop area in which slump folds and slump-related reverse faults are at high angles to transport direction (E and F; cf. A and C, respectively; Debacker and De Meester, 2009). A) Mean fault orientation method; B) fault separation method; C) fault intersection method; D) best-fit girdle to fault poles method. Note that inferred slump direction is variable but slump sense is always roughly towards the south. See text.

internal geometries and may have experienced changes in transport direction (cf. Strachan and Alsop, 2006), smaller error margins should be considered unrealistic.

6.2. Methods based on slump fault data

Contrary to the analysis of recent slumps and slides, in which much attention is paid to faults, slump-related faults have generally been neglected in the analysis of ancient slumps. This is unfortunate, as much information about palaeoslope orientation can be gained from slump-related faults, in particular when used in combination with fold data. The methods proposed below assume that, as for slump folds, also faults – both normal and reverse – have an orientation that is intimately linked to slump transport (e.g. Maltman, 1994; Smith, 2000; Strachan, 2008; Debacker and De Meester, 2009). In all cases, slump sense is taken to be down-dip for (the majority of) normal faults and opposite to the dip direction for (the majority of) reverse faults. An obvious uncertainty is the fact that slip direction indicators are often absent, cannot be observed (e.g. welded faults) or are obscured by later deformation. However, this is not as serious a problem as it may seem. After all, material movement lines are unknown for slump folds too. Given a known relative apparent movement sense, as determined on the basis of kinematic constraints (e.g. drag phenomena) or relative displacement of marker horizons, slump fault data can be used for slump analysis.

We measured the orientation of several slump-related faults, both in outcrop and in oriented hand specimens. For those in outcrop, we only took into account the most apparent ones with a clear sense of apparent displacement (e.g. Fig. 5). Those in oriented hand samples were all encountered by chance, and generally have very small displacements (e.g. Fig. 4A–D). Unlike displacement sense, the amount of displacement and the scale of the faults do not appear to influence the results.

6.2.1. Mean fault orientation method

The rose plot of the normal and reverse faults has a markedly bimodal shape, with a mean of $097^\circ \pm 047^\circ$, seemingly suggestive of southward slumping from $007^\circ \pm 047^\circ$ (Fig. 11A). The normal faults have a mean trend of $067^\circ \pm 032^\circ$, suggestive of southward slumping from $337^\circ \pm 032^\circ$ and being fully compatible with the slump fold data results (Fig. 10). For the reverse faults, a mean trend of $126^\circ \pm 035^\circ$ is obtained, seemingly suggestive of southward slumping from $036^\circ \pm 035^\circ$. This is not compatible with the fold data results.

For comparative purposes, in Fig. 11E data are presented of reverse slump-related faults considered to be situated in the central to frontal parts of a slump sheet of the same stratigraphic unit (Debacker and De Meester, 2009). In contrast to our results, these reverse faults perfectly match the fold-based slump sense and direction.

6.2.2. Fault separation method

This method consists of outlining areas of poles of reverse and normal faults on an equal-area stereographic projection and taking the bisector of each field. For normal faults, the sense of slumping is along the bisector of the area of normal fault poles towards the opposite field, and for reverse faults slump sense is along the bisector of the area of reverse faults poles starting from the opposite field. Ideally, poles to normal and reverse faults occupy opposite fields.

This method becomes complicated when many gently dipping faults occur. In such cases, as in Fig. 11F (Debacker and De Meester, 2009), areas of poles to normal and reverse faults become much larger, and so does the uncertainty on the bisector. In our case, however, the distribution of the poles to both groups of faults leads to satisfying results, being $006^\circ \pm 046^\circ$ for the normal faults and $359^\circ \pm 065^\circ$ for the reverse faults (Fig. 11B). Both results overlap with the fold-based results.

6.2.3. Fault intersection method

This method assumes that the intersection of slump-related faults should be oriented ideally perpendicular to slump transport direction. In case only reverse or normal faults are observed, or in case it is doubtful whether the normal and reverse faults formed by

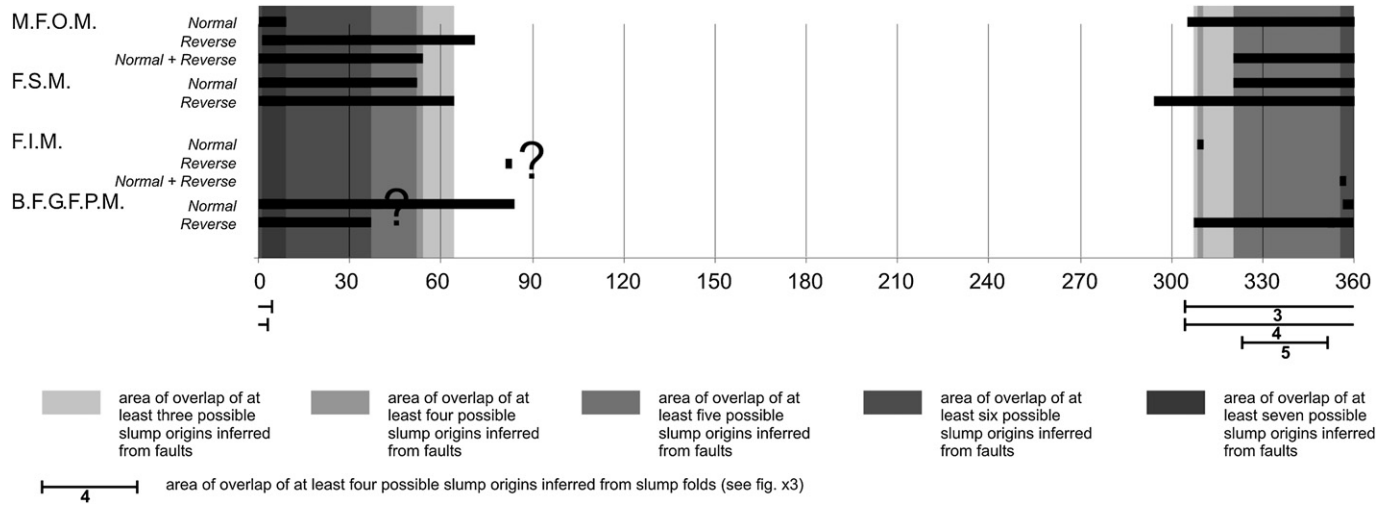

Fig. 12. Summary graph of the four slump fault-based methods employed, with areas of overlap for three, four, five, six and seven results. Also added are the areas of overlap for three, four and five possible slump origins derived from the fold-based methods (see Fig. 10). M.F.O.M.: mean fault orientation method; F.S.M.: fault separation method; F.I.M.: Fault intersection method; B.F.G.F.P.M.: best-fit girdle to fault poles method. See text.

slumping along a similar slope, the intersection of both types of faults is considered separately. For the reference example of Fig. 11F, representative for the central to frontal parts of a slump sheet, the intersection of the reverse faults is subhorizontal and perpendicular to slump transport direction (Debacker and De Meester, 2009).

For the present study, the intersection of the normal faults is 39/219, seemingly suggestive of slumping from 309° to 129°, and the intersection of the reverse faults is 33/352, seemingly suggestive of slumping from 082° to 262° (Fig. 11C). Only the result for the normal faults is roughly compatible with the fold-based results.

On the assumption that the normal and reverse faults formed as a result of the same slumping event, or as a result of consecutive slumping events along a similar slope, the intersection of the mean normal fault plane and the mean reverse fault plane is considered to be subperpendicular to slump transport direction. The intersection (13/086) of the mean normal fault plane (079/61S) and the mean reverse fault plane (281/41N) suggests slumping from 356° to 176°. This is compatible with the fold-based results.

6.2.4. Best-fit girdle to fault poles method

From the above it becomes clear that many faults have an orientation that is not subperpendicular to slump transport direction. This holds true, in particular, for the reverse faults, of which the mean is markedly oblique to the slump direction inferred from slump folds. The present method is related to the bow-and-arrow-method and uses the assumption that the fanning axis of the faults is at low angles to the slump transport direction. Slump sense is down-plunge along the fanning axis for the normal faults (up-dip best-fit girdle) and up-plunge along the fanning axis for the reverse faults (down-dip best-fit girdle). Arbitrarily, we propose an error margin of 045° about the fanning axis plunge direction.

The best-fit girdle to the normal fault poles has an orientation of 309/51N, seemingly suggesting slumping from 039° to 219° (±045°; Fig. 11D). This is not compatible with the slump fold results. The best-fit girdle to the reverse fault poles has an orientation of 082/57S, suggestive of slumping from 352° to 172° (±045°) and being compatible with the fold results.

6.2.5. Comparison of the results

In most cases the results from the slump-related faults overlap with the fold-based results (Fig. 12, compare with Fig. 10). This is the case for the mean of the normal faults and the mean of normal and reverse faults in the mean fault orientation method (Fig. 11A), for both the normal and reverse faults in the fault separation method (Fig. 11B), for the intersection of the normal faults and for the intersection of the mean normal fault plane and mean reverse fault plane in the fault intersection method (Fig. 11C), and for the reverse faults in the best-fit girdle to fault poles method (Fig. 11D). However, for the mean of the reverse faults in the mean fault orientation method (Fig. 11A), for the intersection of the reverse

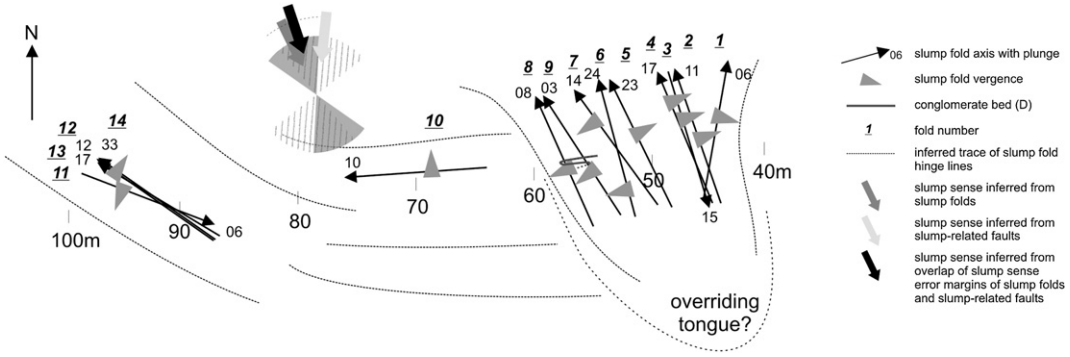

Fig. 13. Orientation and asymmetry of the slump folds, after untilting and unfolding (cf. Fig. 3 and Table 2). Also the deduced slump sense is indicated, as well as an interpretative overall slump geometry, based on inferred traces of slump fold hinge lines.

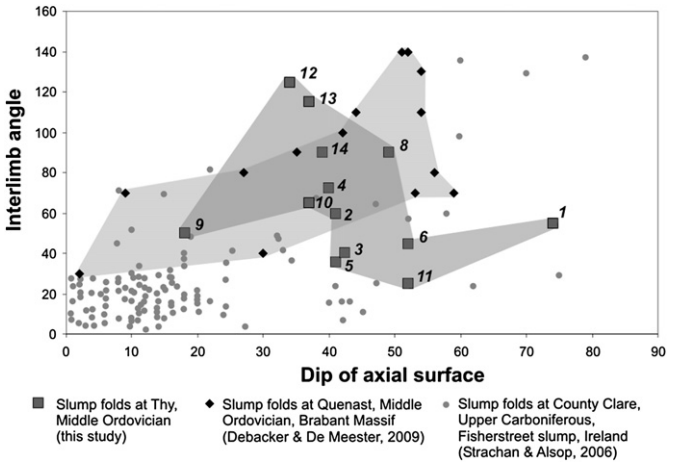

Fig. 14. Graph of interlimb angle versus axial surface dip for the present study, compared with data of Strachan and Alsop (2006) and Debacker and De Meester (2009). In the former case, folds are at low angles to slump transport direction, whereas in the two latter cases, folds are at high angles to slump transport direction. Individual slump folds of the present study are numbered (cf. Tables 1 and 2 and Figs. 3 and 13). See text.

faults in the fault intersection method (Fig. 11C) and for the normal faults in the best-fit girdle to fault poles method (Fig. 11D), the results strongly differ. Although this implies a significant uncertainty regarding the slump direction, the overall slump sense (i.e. from ~N–S) is much more obvious than in the case of the fold-based methods (compare with Fig. 10).

Also here, the overlap in results is investigated. For an overlap of three (006° ± 058°), four (309° and 007 ± 047°) and five (006° ± 046°) fault-based results, the resulting areas show a large overlap with the fold-based slump origin interval. For an overlap of six (016° ± 021°) and seven (005° ± 004°) fault-based results, however, the resulting areas are markedly different from the fold-based slump origin interval. Nevertheless, the mean of each overlap area is fairly similar (005°–016°) and is shifted between 30° and 42° clockwise with respect to the mean of the fold-based slump origin intervals. Taking into account the trade-off between the error margin width and the amount of overlap of the different fault-based results, slumping, as inferred from the fault data, appears to have taken place from ~006° ± 046°.

On the basis of slump folds we have deduced slumping from 335° ± 030°, whereas on the basis of the slump-related faults, slumping seemingly took place from ~006° ± 046°. The zone of overlap of both may be considered as a viable final solution, thus suggesting slumping from ~320°–005° towards ~140°–185°.

7. Discussion

7.1. Regional considerations

Despite the complexity and small nature of the data-set, a combination of different methods does allow deduction of a reliable slump transport direction and sense. Together, the different methods demonstrate a slump transport direction at low angles to slump fold orientation. Because of this, the outcrop under study is considered to expose the lateral to oblique parts of a slump sheet or internal lobe or tongue, dominated by layer-normal shear (Fig. 13). The inferred slump transport is fully compatible with previous results on the same units from other parts of the Brabant Massif. These results, obtained from deformation features thought to have formed in the central to frontal parts of slump sheets, suggest slumping from 320°–350° to 140°–170° (Debacker and De Meester, 2009), and from ~358° towards ~178° (Beckers, 2003, 2004). The current study thus seems to confirm the presence of an S-dipping palaeoslope of regional extent during the late Early to Middle Ordovician in the southern part of the Brabant Massif (cf. Debacker and De Meester, 2009).

7.2. Suggested diagnostic criteria and recommendations

Many methods allow for several possible interpretations. For our data, this concerns in particular the mean axis method, the axial–planar intersection method, the fold hinge azimuth and interlimb angle method and the axial surface strike and interlimb angle method. Moreover, for some methods, such as the separation arc method, no trustworthy solution is obtained. In such cases, these methods on their own are virtually useless for interpreting small complex data-sets. As demonstrated above, however, a rigorous comparison of the results of different methods, using both fold and fault data, and taking into account all assumptions of each single method, can provide a reliable slump transport direction and sense.

In addition, some methods do show some geometrical relationships that may be diagnostic for a specific fold orientation relative to slump transport direction. Having at least some idea of this relative orientation significantly improves the use of any of the other methods, for which different interpretations are possible. Several of these diagnostic criteria are listed below.

For inferring fold-based slump transport direction and sense, we used the assumption that folds become steeper (see 6.1.6; cf. Alsop and Holdsworth, 2007) and become tighter (see 6.1.4 and 6.1.5.; cf. Strachan and Alsop, 2006) as fold axis orientation approaches the slump transport direction. Combined, this suggests that slump folds tighten as they become steeper. On a graph of interlimb angle

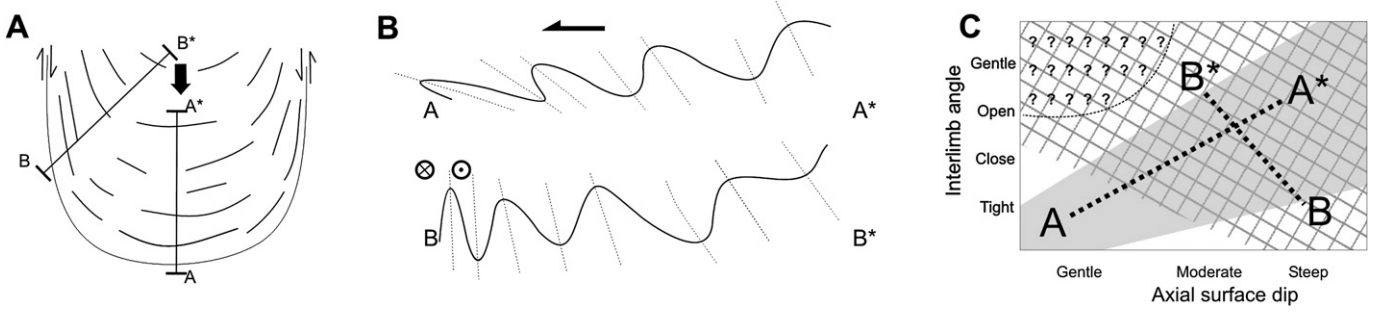

Fig. 15. Schematic representation of bedding and fold geometries at the frontal and lateral margins of a slump sheet. A) Plan view of an idealised slump sheet with associated slump fold hinge lines. Black arrow represents slump transport. B) Two cross-sections along the slump sheet depicted in A, showing idealised bedding and fold geometries across the frontal (A–A*) and lateral parts (B–B*) of the slump sheet (see A for section lines). C) Fold geometries across the frontal (A–A*) and lateral (B–B*) parts of the slump sheet on a graph of interlimb angle versus axial surface dip (see also Fig. 14).

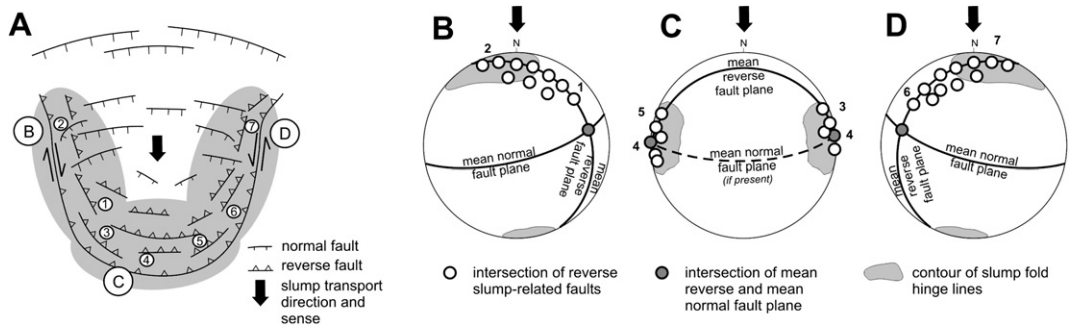

Fig. 16. Fault geometries within the different parts of an idealised slump sheet or lobe. A) Plan view of a S-directed slump sheet or lobe. B–D) Lower-hemisphere equal-area projections showing mean normal and mean reverse fault plane, the intersection lineation of these, the intersection of reverse faults and contours of slump fold hinge lines. In B) data are from the dextrally deformed lateral to oblique parts, in C) from the frontal to oblique parts and in D) from the sinistrally deformed lateral to oblique parts (see A for position). Numbers refer to the orientation of reverse fault intersections at the position shown in A. See text.

versus axial surface dip this is reflected by a rough, negative relationship (Fig. 14). The rough nature of this relationship is likely due to local disturbances such as obliquely stacked beds or strong local competence contrasts (e.g. fold 9 is controlled by conglomerate bed D). By contrast, fabric topology plots of Strachan and Alsop (2006) show a rough, positive relationship: folds become tighter as they become less steep. The latter relationship is also reflected by the data of Debacker and De Meester (2009) (see Fig. 2 for location). Both data-sets, however, are from zones in which no major fold axis rotation occurred – the central to frontal slump parts – whereas the folds of the present study correspond to the lateral to oblique parts of a slump sheet or internal tongue or lobe. Hence, a different relationship appears to exist for folds trending at high angles to slump transport direction as opposed to folds trending at low angles to slump transport direction. Within the frontal parts, dominated by layer-parallel shear, folds tighten as the axial surface dip decreases, whereas in the lateral parts, dominated by layer-normal shear, the folds tighten and the axial surfaces become steeper as the fold hinges become closer to the slump transport direction (Fig. 15). If correct, this may be used as a diagnostic criterion (cf. Alsop and Holdsworth, 2004, 2007). Such a criterion greatly benefits the interpretation of methods such as the mean axis method, for which it may be difficult to tell whether down-slope or along-slope average axes are observed.

One of the major advantages of the fault-based methods lies in the fact that the broad slump sense can be fairly easily determined, even though the actual slump direction may be difficult to deduce. Also this will largely reduce the number of possible interpretations of other methods. For the mean axis method, for instance, this reduces the number of possible slump directions from four to two (compare Fig. 7A and Fig. 12).

Within the lateral to oblique parts of a slump sheet or internal lobe, reverse faults are at moderate to low angles to slump transport direction, whereas within the frontal parts they are at high angles to transport direction. If the fanning axis (β-axis) of the reverse faults is subhorizontal and approximates the mean fold axis orientation of a subhorizontal, tightly clustered group of slump folds (cf. Debacker and De Meester, 2009; Fig. 11F), folds and faults are more likely to be oriented at high angles to slump transport direction, and probably correspond to the frontal to central parts of the slump sheet or internal lobe (Fig. 16C). In such cases, the fault intersection method should give reliable results, with slump direction being subperpendicular to the reverse faults fanning axis, and slump sense being opposite to the dip direction of the mean reverse fault. By contrast, if the fanning axis (β-axis) of the reverse faults has a significant plunge, a position within the lateral to oblique parts of a slump sheet or internal lobe is more likely (Fig. 16B and D). The fanning axis orientation may parallel or may deviate from the mean slump fold axis, and the fold axes are not expected to be tightly clustered. In such cases, the best-fit girdle to fault poles method is suitable for restraining slump sense and direction. The plunge of the reverse faults fanning axis opposes the slump sense, and transport direction may be subparallel to oblique to the fanning axis, but will not be perpendicular to it.

The plunge azimuth of the intersection of the normal and reverse faults may be used for determining whether the data are from the dextrally or sinistrally deformed lateral to oblique parts (Fig. 16). Within the dextrally deformed parts (i.e. W-part for a S-directed slump), the intersection of the reverse and normal faults is expected to be oriented at high angles to the slump transport direction, with a plunge azimuth oriented anticlockwise with respect to slump sense (i.e. to E for a S-directed slump; Fig. 16B). Within the sinistrally deformed parts (i.e. E-part for a S-directed slump), the plunge azimuth of the intersection is expected to be oriented clockwise with respect to slump sense (i.e. to W for a S-directed slump; Fig. 16D). For our data, this approach suggests a position within the western, dextrally deformed lateral to oblique parts of a S-directed slump sheet or internal tongue or lobe (compare with Fig. 13). Also the observed discrepancy between slump transport direction inferred from slump folds as opposed to that inferred from slump-related faults may be explained in a similar way (see Figs. 12, 13 and 16). Within the dextrally deformed parts, slump transport direction inferred from faults is oriented clockwise with respect to that inferred from folds (as observed; see Fig. 12), whereas in the sinistrally deformed parts, an anticlockwise relationship is expected.

8. Conclusions

Even for small complex data-sets of slump deformation features, reliable information can be obtained about slump transport direction and sense, provided (a) as many methods as possible are used and (b) the results of these are compared in a rigorous way. In addition, not only slump fold data, but also slump-related fault data should be incorporated. Slump-related fault data do provide valuable information about slump transport direction and sense. When these fault data are combined with slump fold data, inferred slump transport direction becomes much more reliable. Moreover, several possible diagnostic criteria are proposed for the frontal to central and lateral to oblique parts of slump sheets or internal lobes or tongues.

The present results indicate slumping from $\sim 335^\circ \pm 030^\circ$ for the fold-based methods and from $\sim 006^\circ \pm 046^\circ$ for the fault-based methods. Combined, this suggests slumping from $\sim 320^\circ$–005°

towards ~140°–185°. This is fully compatible with previous results on the same stratigraphic levels from other outcrop areas of the Brabant Massif, and seems to confirm the presence of a late Early to Middle Ordovician S-dipping palaeoslope of regional extent.

The combination of the results of the different fold- and fault-based methods leads to a slump transport direction error margin that is higher than that of some of the individual methods. However, at the same time, the reliability of the final result significantly improves. When dealing with slump deformation features, it should be realised that slump directions with an accuracy of less than 10°, as often inferred from individual methods, are geologically unrealistic. The combination of the different methods proposed herein does lead to robust results, with a geologically realistic error margin, even for small complex data-sets.

Acknowledgements

We kindly acknowledge I. Alsop and an anonymous reviewer for thoroughly reviewing the manuscript and editor R.E. Holdsworth for the professional handling of the manuscript. We would also like to thank A. Herbosch, J. Verniers and N. Woodcock for helpful discussions. The first author is also grateful to M. and A. Debacker for the stimulating environment. T.N. Debacker is a Postdoctoral Fellow of the Fund for Scientific Research-Flanders (F.W.O.-Vlaanderen). This work forms part of research project G.0271.05 of the F.W.O.-Vlaanderen.

References

Alsop, G.I., Holdsworth, R.E., 2002. The geometry and kinematics of flow perturbation folds. Tectonophysics 350, 99–125.

Alsop, G.I., Holdsworth, R.E., 2004. Shear zone folds: records of flow perturbation or structural inheritance? In: Alsop, G.I., Holdsworth, R.E., McCaffrey, K.J.W., Hand, M. (Eds.), Flow Processes in Faults and Shear Zones Geological Society, London, Special Publications, vol. 224, pp. 177–199.

Alsop, G.I., Holdsworth, R.E., 2007. Flow perturbation folding in shear zones. In: Ries, A.C., Butler, R.W.H., Graham, R.D. (Eds.), Deformation of the Continental Crust: The legacy of Mike Coward. Geological Society, London, Special Publications, vol. 272, pp. 77–103.

Beckers, R., 2003. Vergelijking van de plooien in de Abbaye de Villers en Chevlipont formaties (Ordovicium) in de omgeving van de Abdij van Villers, Thyle-vallei, Massief van Brabant. Unpublished M.Sc.-thesis, Universiteit Gent.

Beckers, R., 2004. Comparison of folds in the Chevlipont and Abbaye de Villers Formations, near the abbey of Villers, Thyle valley, Brabant Massif. Geologica Belgica 7, 357–359.

Beckers, R., Debacker, T.N., 2006. Influence of slump folds on tectonic folds: an example from the Lower Ordovician of the Anglo-Brabant Deformation Belt, Belgium. Journal of the Geological Society of London 163, 37–46.

Blay, P., Cosgrove, J.W., Summers, J.M., 1977. An experimental investigation of the development of structures in multilayers under the influence of gravity. Journal of the Geological Society of London 133, 329–342.

Bradley, D., Hanson, L., 1998. Paleoslope analysis of slump folds in the Devonian Flysch of Maine. Journal of Geology 106, 305–318.

Carney, J.N., Alexandre, P., Pringle, M.S., Pharaoh, T.C., Merriman, R.J., Kemp, S.J., 2008. 40Ar–39Ar isotope constraints on the age of deformation in Charnwood Forest, UK. Geological Magazine 145, 702–713.

Corbett, K.D., 1973. Open-cast slump sheets and their relationship to sandstone beds in an Upper Cambrian flysch sequence, Tasmania. Journal of Sedimentary Petrology 43, 147–159.

Coward, M.P., Kim, J.H., 1981. Strain within thrust sheets. In: McClay, K.R., Price, N.J. (Eds.), Thrust and Nappe Tectonics. Geological Society, London, Special Publications, vol. 9, pp. 275–292.

Coward, M.P., Potts, G.J., 1983. Complex strain patterns developed at the frontal and lateral tips to shear zones and thrust zones. Journal of Structural Geology 5, 383–399.

Crimes, T.P., 1970. A facies analysis of the Cambrian of Wales. Palaeogeography Palaeoclimatology Palaeoecology 7, 113–170.

Debacker, T.N., 2001. Palaeozoic deformation of the Brabant Massif within eastern Avalonia: how, when and why? Unpublished Ph.D.-thesis, Universiteit Gent.

Debacker, T.N., De Meester, E., 2009. A regional, S-dipping late Early to Middle Ordovician palaeoslope in the Brabant Massif, as indicated by slump folds (Anglo-Brabant Deformation Belt, Belgium). Geologica Belgica 12, 145–159.

Debacker, T.N., Dewaele, S., Sintubin, M., Verniers, J., Muchez, Ph., Boven, A., 2005a. Timing and duration of the progressive deformation of the Brabant Massif, Belgium. Geologica Belgica 8, 20–34.

Debacker, T.N., Herbosch, A., Sintubin, M., 2005b. The supposed thrust fault in the Dyle–Thyle outcrop area (southern Brabant Massif, Belgium) re-interpreted as a folded low-angle extensional detachment. Geologica Belgica 8, 53–69.

Debacker, T.N., Herbosch, A., Sintubin, M., Verniers, J., 2003. Palaeozoic deformation history of the Asquempont-Virginal area (Brabant Massif, Belgium). Memoirs of the Geological Survey of Belgium 49, 1–30.

Debacker, T.N., Sintubin, M., Verniers, J., 2001. Large-scale slumping deduced from structural and sedimentary features in the Lower Palaeozoic Anglo-Brabant fold belt, Belgium. Journal of the Geological Society of London 158, 341–352.

Debacker, T.N., van Noorden, M., Sintubin, M., 2006. Distinguishing syn-cleavage folds from pre-cleavage folds to which cleavage is virtually axial planar: examples from the Cambrian core of the Lower Palaeozoic Anglo-Brabant Deformation Belt (Belgium). Journal of Structural Geology 28, 1123–1138.

de Magnée, I., Lambeau, J., 1965. Le grés poudingue phosphatifère et manganesifère de Thy (Vallée de la Dyle). Bulletin de la Société belge de Géologie, de Paléontologie et d'Hydrologie 74, 293–300.

De Vos, W., Verniers, J., Herbosch, A., Vanguestaine, M., 1993. A new geological map of the Brabant Massif, Belgium. Geological Magazine 130, 605–611.

Elliott, C.G., Williams, P.F., 1988. Sediment slump structures: a review of diagnostic criteria and application to an example from Newfoundland. Journal of Structural Geology 10, 171–182.

Farrell, S.G., 1984. A dislocation model applied to slump structures, Ainsa Basin, South Central Pyrenees. Journal of Structural Geology 6, 727–736.

Farrell, S.G., Eaton, S., 1987. Slump strain in the tertiary of Cyprus and the Spanish Pyrenees. Definition of palaeoslopes and models of soft-sediment deformation. In: Jones, M.E., Preston, R.M.F. (Eds.), Deformation of Sediments and Sedimentary Rocks. Geological Society, London, Special Publications, vol. 29, pp. 181–196.

Hahn, F., 1913. Untermeerische gleitung bei Trenton falls (Nord-America) und ihr Verhaltnis zu ahnlinchen storungsbildern. Neues Jahrbuch Mineralogie, Beilage Bd. 36, 1–41.

Hansen, E., 1965. Methods of deducing slip-line orientations from the geometry of folds. Year Book of the Carnegy Institute Washington 65, 387–405.

Hansen, E., 1967. Natural slip folds in which the fold axes nearly parallel the slip lines. Year Book of the Carnegy Institute Washington 66, 536–538.

Hansen, E., 1971. Strain Facies. Springer-Verlag, New York.

Helwig, J., 1970. Slump folds and early structures, northeastern Newfoundland Appalachians. Journal of Geology 78, 172–187.

Herbosch, A., Lemonne, E., 2000. Carte Nivelles-Genappe no 39/7-8, Carte géologique de Wallonie, échelle 1/25000. Ministère de la Région Wallonne, Namur.

Herbosch, A., Vanguestaine, M., 1994. La Formation de Mousty et nouvelle interprétation du Chemin creux de Thy. In: Excursion guide 17th novembre 1994, organised by groupe de contact F.N.R.S.: "Geologie des massifs Calédoniens".

Herbosch, A., Vanguestaine, M., Degardin, J.M., Dejonghe, L., Fagel, N., Servais, T., 1991. Etude lithostratigraphique, biostratigraphique et sédimentologique du sondage de Lessines (bord méridional du Massif du Brabant, Belgique). Annales de la Société Géologique de Belgique 114, 195–212.

Jones, O.T., 1939. The geology of the Colwyn Bay district: a study of submarine slumping during the Salopian Period. Quarterly Journal of the Geological Society of London 95, 335–382.

Kuenen, Ph.H., 1949. Slumping in the Carboniferous rocks of Pembrokeshire. Quarterly Journal of the Geological Society of London 104, 365–380.

Lajoie, J., 1972. Slump fold axis orientations: an indication of paleoslope? Journal of Sedimentary Petrology 42, 584–586.

Legrand, R., 1968. Le Massif du Brabant. Mémoires pour servir à l'Explication des Cartes Géologiques et Minières de la Belgique 9, 1–148.

Maltman, A., 1994. The Geological Deformation of Sediments. Chapman & Hall, London.

Michot, P., 1977. L'Ordovicien de la vallée de la Thyle (Brabant): structure tectonique, stratigraphie et lithologie. Annales de la Société Géologique de Belgique 100, 223–231.

Parnell, J., 2009. Global mass wasting at continental margins during Ordovician high meteorite influx. Nature 2, 57–61.

Rupke, N.A., 1976. Large-scale slumping in a flysch basin, Southwestern Pyrenees. Journal of the Geological Society of London 132, 121–130.

Sintubin, M., 1997. Cleavage–fold relationships in the Lower Paleozoic Brabant Massif (Belgium). Aardkundige Mededelingen 8, 161–164.

Sintubin, M., 1999. Arcuate fold and cleavage patterns in the southeastern part of the Anglo-Brabant Fold Belt (Belgium): tectonic implications. Tectonophysics 309, 81–97.

Smith, J.V., 2000. Flow pattern within a Permian submarine slump recorded by oblique folds and deformed fossils, Ulladulla, south-eastern Australia. Sedimentology 47, 357–366.

Strachan, L.J., 2008. Flow transformations in slumps: a case study from the Waitemata Basin, New Zealand. Sedimentology 55, 1311–1332.

Strachan, L.J., Alsop, G.I., 2006. Slump folds as estimators of palaeoslope: a case study from the Fisherstreet Slump of County Clare, Ireland. Basin Research 18, 451–470.

Van Grootel, G., Verniers, J., Geerkens, B., Laduron, D., Verhaeren, M., Hertogen, J., De Vos, W., 1997. Timing of subsidence-related magmatism, foreland basin development, metamorphism and inversion in the Anglo-Brabant fold belt. Geological Magazine 134, 607–616.

Vanmeirhaeghe, J., 2006. The evolution of the Condroz-Brabant Basin from Middle Ordovician to Llandovery: lithostratigraphical and chitinozoan biostratigraphical approach. Unpublished Ph.D.-thesis, Universiteit Gent.

Verniers, J., Herbosch, A., Vanguestaine, M., Geukens, F., Delcambre, B., Pingot, J.L., Belanger, I., Hennebert, M., Debacker, T., Sintubin, M., De Vos, W., 2001. Cambrian–Ordovician–Silurian lithostratigraphic units (Belgium). Geologica Belgica 4, 5–38.

Verniers, J., Pharaoh, T., André, L., Debacker, T., De Vos, W., Everaerts, M., Herbosch, A., Samuelsson, J., Sintubin, M., Vecoli, M., 2002. The Cambrian to mid Devonian basin development and deformation history of Eastern Avalonia, east of the Midlands Microcraton: new data and a review. In: Winchester, J., Pharaoh, T., Verniers, J. (Eds.), Palaeozoic Amalgamation of Central Europe. Geological Society, London, Special Publications, vol. 201, pp. 47–93.

Wheeler, R.L., 1975. Kinematic tests of multiple working hypotheses for the origin of contorted zones, Marcellus Formation, eastern Plateau Province, West Virginia. Abstracts and Program, Geological Society of America 7, 132–133.

Woodcock, N.H., 1976a. Structural style in slump sheets: Ludlow Series, Powys, Wales. Journal of the Geological Society of London 132, 399–415.

Woodcock, N.H., 1976b. Ludlow Series slumps and turbidites and the form of the Montgomery Trough, Powys, Wales. Proceedings of the Geologists Association 87, 169–182.

Woodcock, N.H., 1979. The use of slump structures as palaeoslope orientation estimators. Sedimentology 26, 83–99.